Influence of Travelling Current Linkage Harmonics on Inductance Variation, Torque Ripple and Sensorless Capability of Tooth-Coil Permanent Magnet Synchronous Machines

Pavel Ponomarev, *Member, IEEE*, Ilya Petrov, Juha Pyrhönen, *Member, IEEE*

Laboratory of Electrical Drives Technology, Lappeenranta University of Technology, 53850 Lappeenranta, Finland.

This paper introduces an important source of torque ripple in PMSMs with tooth-coil windings (TC-PMSMs). It is theoretically proven that saturation and cross-saturation phenomena caused by the non-synchronous harmonics of the stator current linkage cause a synchronous inductance variation with a particular periodicity. This, in turn, determines the magnitude of the torque ripple and can also deteriorate the performance of signal-injection-based rotor position estimation algorithms. An improved *dq*- inductance model is proposed. It can be used in torque ripple reduction control schemes and can enhance the self-sensing capabilities of TC-PMSMs.

***Index Terms*—Current linkage harmonics, high torque density, inductance model, permanent magnet machines, TC-PMSM, tooth-coil winding, torque ripple, saturation, sensorless control.**

I. Introduction

THE *dq*-model, or rotor flux oriented model for rotating AC electrical machines, was originally introduced to simplify the analysis and control of multi-phase electric motor drives. It significantly reduces the number of control variables. The *dq*-model is the enabling technique for controlled AC machine drives and the most important concept to understanding how field-oriented control works.

After the transformation of 3-phase quantities to the *dq*-quantities the voltages are defined by a two-component vector U_{dq} instead of a 3-component vector U_{UVW}. The vector model of a PMSM in the rotor-flux-oriented frame (*dq*-coordinates) consists of equations (1)–(5)

$$U_{\mathrm{d}} = R_{\mathrm{s}} i_{\mathrm{d}} + \frac{\mathrm{d}\Psi_{\mathrm{d}}}{\mathrm{d}t} - \omega \Psi_{\mathrm{q}}, \tag{1}$$

$$U_{\mathrm{q}} = R_{\mathrm{s}} i_{\mathrm{q}} + \frac{\mathrm{d}\Psi_{\mathrm{q}}}{\mathrm{d}t} + \omega \Psi_{\mathrm{d}}, \tag{2}$$

$$T_{\mathrm{e}} = \frac{3}{2} p (\Psi_{\mathrm{d}} i_{\mathrm{q}} - \Psi_{\mathrm{q}} i_{\mathrm{d}}), \tag{3}$$

$$\Psi_{\mathrm{d}} = L_{\mathrm{d}} i_{\mathrm{d}} + \Psi_{\mathrm{PM}}, \tag{4}$$

$$\Psi_{\mathrm{q}} = L_{\mathrm{q}} i_{\mathrm{q}}. \tag{5}$$

where U_{d} and U_{q} are the *d*- and *q*-axis components of the stator voltage, Ψ_{d} and Ψ_{q} are the *d*- and *q*-axis components of the airgap flux linkage, T_{e} is the electromagnetic torque, i_{d} and i_{q} are the *d*- and *q*-axis components of the stator current and Ψ_{PM} is the permanent magnet flux linkage.

The *dq*-model is widely used in electrical drives. The vector control and field-oriented control techniques take their origins from the *dq*-model of the machine.

There are several assumptions under which the *dq*-transformation is valid:

- materials have linear characteristics (no saturation),
- windings are assumed to create sinusoidal waveforms for flux densities, flux linkages, and back-EMFs, being supplied with sinusoidal currents.

Such assumptions are quite well valid for three-phase integral slot winding machines, however, tooth-coil windings produce significant amounts of current linkage harmonics, which rotate asynchronously with the rotor and may locally saturate iron core.

The analysis of a Tooth-Coil Permanent Magnet Synchronous Machine (TC-PMSM) can be based on a fact that the operation of the machine takes place not at the fundamental current linkage harmonic, but at a higher order harmonic. In case of a 9/8 machine (base machine for 18/16) the operating (synchronous) harmonic is the 4^{th} one. Correspondingly, in a 12/10-machine the operating harmonic is the 5^{th} harmonic. The frequencies and the pole pitches of these synchronous harmonics correspond to the frequencies and pole pitches of the rotor-created travelling flux linkage waveforms.

Fig. 1 shows the current linkage harmonics of a 9/8 double layer TC-PMSM – the base machine for the 18/16 TC-PMSM [1]. The spectrum includes the magnitude of the main working harmonic, which is the 4^{th}, and the magnitudes of other current linkage travelling harmonics in the air gap. The relative strengths of the first and the second harmonics – the sub-harmonics rotating faster than the operating harmonic – are high enough to cause adverse effects in the machine [2].

The waves of the current linkage harmonics spectrum for a 9/8 TC-PMSM at a time instant when $i_{\mathrm{U}} = 1$ A, $i_{\mathrm{V}} = -0.5$ A and $i_{\mathrm{W}} = -0.5$ A are illustrated in Fig. 2. During sinusoidal current supply these current linkage harmonics have the same angular speed as the main working harmonic. However, because of the fact that their pole pitches are different, the rotation speed along the stator bore of the harmonic with the lowest order is the fastest (e.g. if the 4^{th} harmonic has travelled once around the circumference, the 1^{st} has rotated four times

Manuscript received May 08, 2013; revised Sep. 02, 2013.
e-mail: name.surname@lut.fi

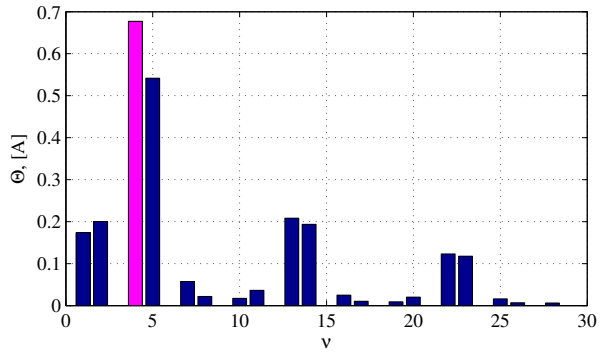

Fig. 1. Current linkage harmonics of a 9/8 machine.

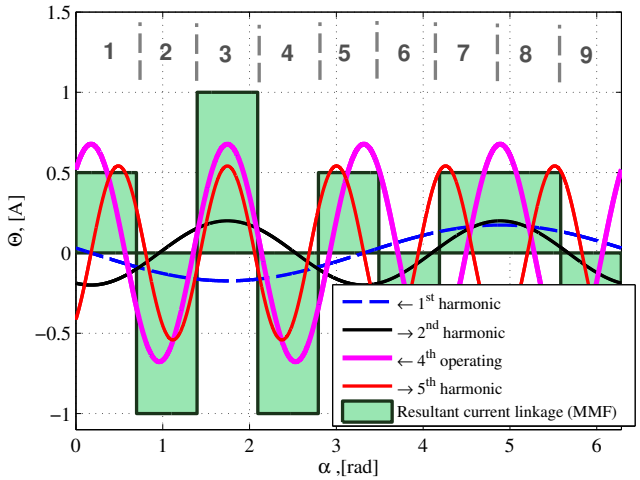

Fig. 2. Travelling current linkage harmonic waves in the air gap of a 9/8 machine. $i_{\mathrm{U}} = 1$ A, $i_{\mathrm{V}} = -0.5$ A and $i_{\mathrm{W}} = -0.5$ A. Tooth numbers are shown above the waveforms.

around the circumference). The sub-harmonics have the widest pole pitches and, therefore, tend to penetrate deep in the rotor. Having high speed on the rotor surface the sub-harmonics easily cause a lot of losses in conducting parts of the rotor. Therefore, as it was also proven in [3], the current linkage sub-harmonics are the main cause of the losses in the rotor and the permanent magnets. However, the main objective of this article is not the estimation of the losses due to asynchronous harmonics, but the analysis of the influence of these harmonics on the synchronous inductance and, consequently, on the electromagnetic torque quality (smoothness).

The synchronous harmonic order of a 9/8 TC-PMSM is $\nu = 4$ and harmonic travels to the positive direction with the rotor. The 1^{st} harmonic and the 7^{th} also travel to the positive direction, whereas, the 2^{nd} and 5^{th} harmonics travel to the opposite direction.

In this paper it is shown that saturation and cross-saturation should be included in the *dq*-model of TC-PMSMs, especially for high-torque-density TC-PMSMs, in order to model their behaviour completely. It is also indicated that the saturation due to the asynchronously-rotating low-order current linkage harmonics produces a considerable torque ripple (5% at the nominal point of the analysed TC-PMSM).

Section II describes saturation and cross-saturation effects in TC-PMSMs. Section III discusses the influence of saturation and cross-saturation on the use of the high-frequency

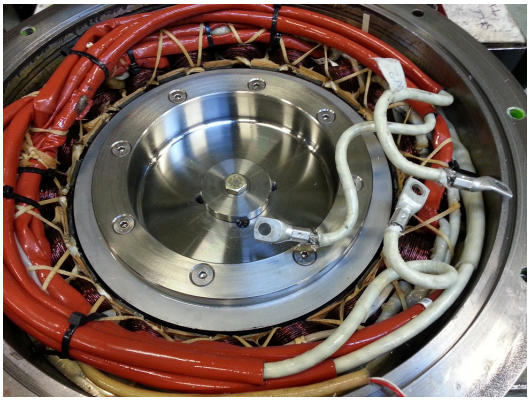

Fig. 3. A photograph of the inside of the 18/16 machine.

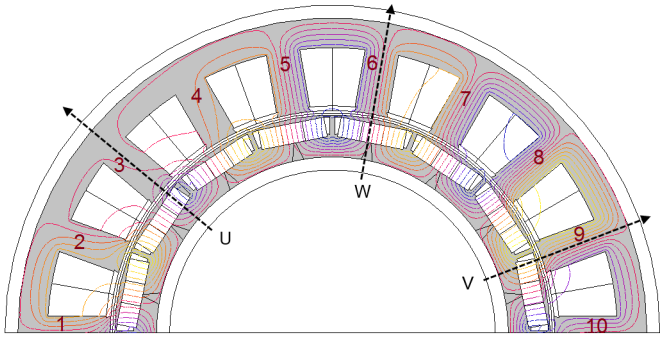

Fig. 4. The modelled 9/8 base machine of the 18/16 machine with flux lines at full loading conditions (i_{d} = -30 A, i_{q} = 120 A). FEM modeling, Rotangle $\Theta = 0$. None of the phase magnetic axes are ideally aligned with the magnetic axes of the rotor. Even though there is the fundamental present in the flux it is so weak that it cannot been observed in the plot. Teeth are numbered.

signal-injection methods in sensorless (or self-sensing) control. Section IV explains that the classical inductance model is not reliable enough when applied to TC-PMSMs; the variation of the synchronous inductance with the rotor position should be also considered for this type of machines. Section V explains that the inductance variation is the main cause for the torque ripple in TC-PMSMs. Finally, Section VI shows approaches to take into account this inductance variation during the design of a TC-PMSM and using an improved *dq*-model.

Examples and FEM modeling are given for an 18/16 TC-IPMSM which was reported in earlier publications [1], [4]. The outlines of this machine are shown in Fig. 3 and Fig. 4.

II. Role of Saturation and Cross Saturation

In real machines the electrical steel lamination is subjected to saturation. Therefore, the first assumption in the *dq*-model is not fulfilled. Usage of such electrical steel imposes the non-linear dependency of magnetic flux linkage on the armature current. It means that the synchronous inductances along the *d*- and *q*-axes are not constants and depend on the magnetic state of the machine [5]. Usually, this effect is ignored and vector control of electric motor drives is implemented with the assumption that the *d*- and *q*- synchronous inductances are constants. However, in cases where variable speeds and torques are required (e.g. in traction applications), saturation can have a dramatic effect on the torque ripple at low speeds, or in the field-weakening region [6].

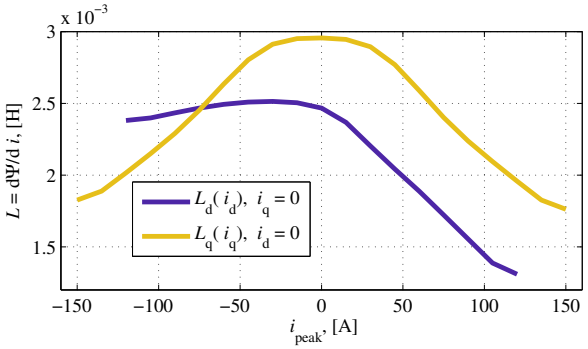

Fig. 5. Inductance variations due to the saturation effect. FEM modeling. Sinusoidal current supply.

A. Saturation

The d-axis current i_d influences the saturation along the d-axis flux path which, in turn, changes the d-axis synchronous inductance L_d of the machine. The same is valid also for q-axis current i_q and the q-axis inductance L_q. Also cross-saturation is present.

When dealing with the non-linear saturation effect the machine model should use differential (incremental) inductances which better represent the local changes of the flux linkages $\partial\Psi_\mathrm{d,q}$ depending on the current changes $\partial i_\mathrm{d,q}$ [7]. The differential inductances can be derived according to

$$L_\mathrm{d,q} = \frac{\partial\Psi_\mathrm{d,q}(i_\mathrm{d,q})}{\partial i_\mathrm{d,q}} \approx \frac{\triangle\Psi_\mathrm{d,q}(i_\mathrm{d,q})}{\triangle i_\mathrm{d,q}}. \tag{6}$$

Fig. 5 shows the L_d and L_q inductances behavior due to the saturation effect. The plots are obtained by linearization of differential inductances with discretization on a grid of the peak phase current with a step of $\triangle i_\mathrm{d,q} = 15$ A.

These direct and quadrature inductance values $L_\mathrm{d}(i_\mathrm{d})$ and $L_\mathrm{q}(i_\mathrm{q})$ can be embedded into the machine model and, therefore, the saturation effect can be taken into account. In this case the model equations (4) and (5) look as follows

$$\Psi_\mathrm{d} = L_\mathrm{d}(i_\mathrm{d})i_\mathrm{d} + \Psi_\mathrm{PM}(i_\mathrm{d}, i_\mathrm{q}), \tag{7}$$

$$\Psi_\mathrm{q} = L_\mathrm{q}(i_\mathrm{q})i_\mathrm{q}. \tag{8}$$

It should be noted that the Ψ_PM is also dependent on the level of saturation and is a function of the current. However, the influence of saturation on PM flux linkage and back-EMF is not the main scope of this study. This influence is very complex and strongly depends on the operating point. Separate study should cover the influence of saturation and cross-saturation on the back-EMF and torque production in order to build an accurate model according to (7). In this paper the back-EMF (and Ψ_PM) variation is not studied. Only the inductance variation is under the scope.

Modern controllers of PMSMs can have dq-inductances stored in look-up tables in the memory [7].

B. Cross-saturation

As shown in [5] in PMSMs the individual axis analysis is not sufficient for accurate modeling. There is also a cross-saturation effect [8] when dq-axes inductances depend on both current components i_d and i_q simultaneously. It happens

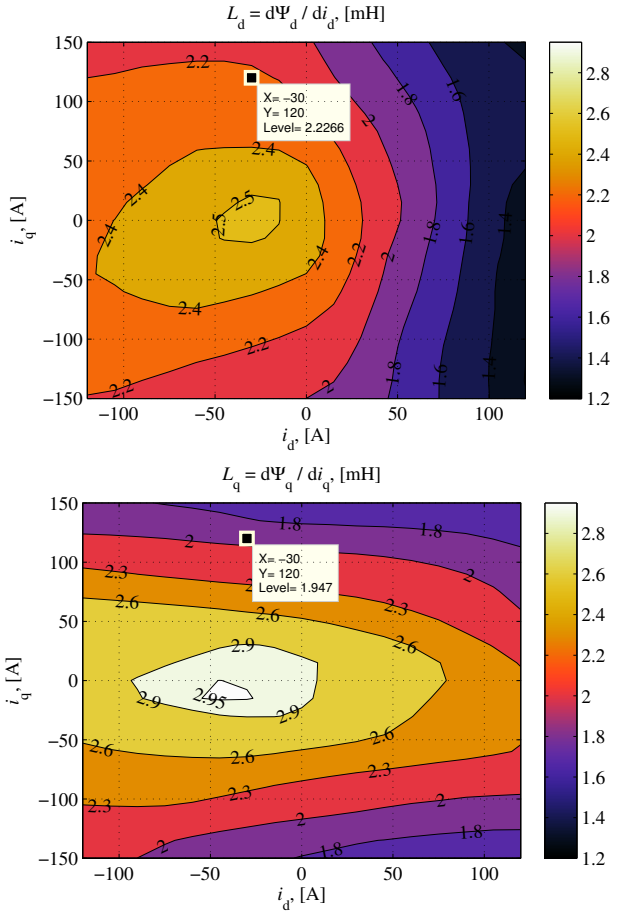

Fig. 6. Direct-axis synchronous differential inductance L_d (top) and quadrature-axis synchronous differential inductance L_q (bottom) maps taking saturation and cross-saturation effects into account. FEM modeling. Rotor position is the same as shown in Fig. 4. Inductance maps are not symmetrical relatively d-axis. Length of a current vector in $i_\mathrm{d}, i_\mathrm{q}$-plane corresponds to the peak phase sinusoidal current.

because, e.g. the q-axis current can saturate direct magnetic axis and d-axis current can influence the magnetic state of the q-axis. Therefore, the cross-saturation effect should be taken into account by calculating the dq-inductances as functions of two variables according to

$$L_\mathrm{d,q} = \frac{\partial\Psi_\mathrm{d,q}(i_\mathrm{d,q}, i_\mathrm{q,d})}{\partial i_\mathrm{d,q}} \approx \frac{\triangle\Psi_\mathrm{d,q}(i_\mathrm{d,q}, i_\mathrm{q,d})}{\triangle i_\mathrm{d,q}}. \tag{9}$$

Fig. 6 shows inductance maps (plots from functions of two variables) obtained by (9) where fluxes and currents are simulated using FEM. Values are obtained by linearization of the differential inductances at operating points with the step size $\triangle i_\mathrm{d,q} = 15$ A of peak phase current.

It can be noticed that the q-axis synchronous inductance L_q saturates fast with increasing q-axis current. This is a result of the thin iron webs between the magnets in the rotor construction as it can be seen in Fig. 4.

With 3-dimensional look-up tables of $L_\mathrm{d}(i_\mathrm{d}, i_\mathrm{q})$ and $L_\mathrm{q}(i_\mathrm{q}, i_\mathrm{d})$ stored in the memory of the motor drive controller, the saturation and cross-saturation effects can be taken into account, and optimal control trajectories (e.g. Maximum Torque per Ampere (MTPA) or Maximum Efficiency Control) can be calculated [9], [10]. The behavior of a PMSM can be precisely

predicted [5]. Flux equations (4) and (5) take a form of

$$\Psi_{\mathrm{d}} = L_{\mathrm{d}}(i_{\mathrm{d}}, i_{\mathrm{q}})i_{\mathrm{d}} + \Psi_{\mathrm{PM}}(i_{\mathrm{d}}, i_{\mathrm{q}}), \tag{10}$$

$$\Psi_{\mathrm{q}} = L_{\mathrm{q}}(i_{\mathrm{q}}, i_{\mathrm{d}})i_{\mathrm{q}}. \tag{11}$$

The permanent magnet flux linkage Ψ_{PM} can be also influenced by the cross-saturation, hence, it is a function of the currents i_{d} and i_{q}.

III. Sensorless Capability

The saturation effect should be carefully considered in case of sensorless (or self-sensing) control. Many sensorless signal-injection control schemes rely on the inductance ratio $\zeta = L_{\mathrm{q}}/L_{\mathrm{d}}$ which should considerably differ from 1 at the whole region of operation [11]. But, as can be seen in Fig. 7 and Fig. 8, at certain values of *d*- and *q*-currents the inductance ratio becomes very close to 1 (values of *d*- and *q*-inductances become very close to each other).

Fig. 7 shows the intersection of the direct and quadrature axis inductance surfaces. At the line of intersection the inversion occurs. At the inversion point the L_{d} axis inductance becomes higher than the L_{q} inductance because of the saturation effects. At this point the sensorless signal-injection control may fail due to the loss of observability. Therefore, in the region of inversion a low-speed sensorless operation of the drive should be forbidden, as in this region only back-EMF-tracking-based sensorless schemes will work. But EMF-based methods of sensorless control fail at zero and low speeds [12]. Therefore, if a low- or zero-speed sensorless control is required, the inversion region should be forbidden in the machine design or operation.

In order to ensure for the described TC-PMSM that the inductance ratio is higher than one within the whole range of intended sensorless operation, the L_{q} axis inductance should be high enough [13]. Therefore, the thickness of the iron web between the poles should be increased [14] in order to make the saliency inversion occur at higher values of the *q*-axis current well above the intended operation region.

As it is seen in Fig. 7 and Fig. 8 the saliency inversion happens when the *q*-axis component of the stator current is close to its nominal value. This is the point at which the PMSM obtains its nominal torque. Therefore, if an electric machine has a similar inductance maps as illustrated in the Fig. 7, and if sensorless field-oriented control is implemented, then, the maximum torque should be reduced to the point where reverse saliency is apparent [15], even if there is still a current reserve from the thermal capability point of view. Alternatively, the low-speed sensorless operation should be forbidden, and back-EMF-based sensorless technique should be used in that region.

Measurement noise, distortion of injected signals, manufacturing unidealities, and dependence of PM flux – and consequently the saturation – from the thermal conditions require widening of the forbidden region in order to ensure the minimum ratio of detectable saliency [11]. Fig. 8 shows the forbidden region for sensorless control using high-frequency signal-injection with 10 % safety limit ($0.9 < \zeta < 1.1$).

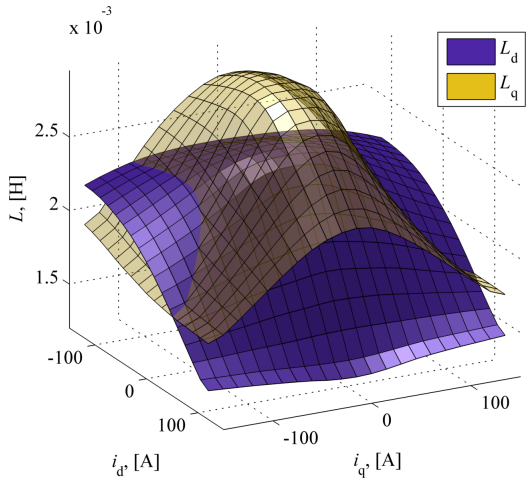

Fig. 7. Intersection of the *d*- and *q*-axis inductances. FEM modeling. Operation near the lines of intersection is not recommended for sensorless control.

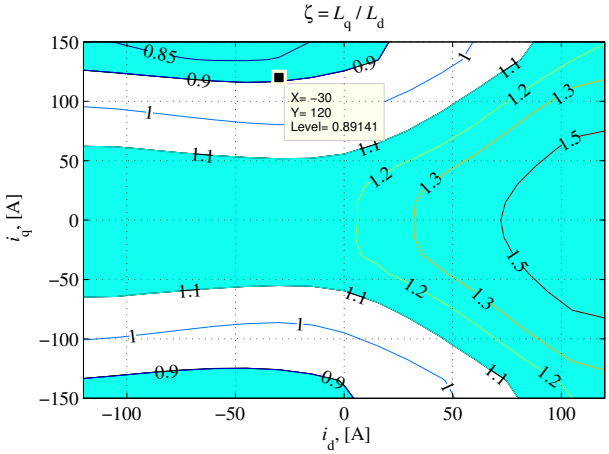

Fig. 8. Forbidden region $0.9 < L_{\mathrm{q}}/L_{\mathrm{d}} < 1.1$ (white) for sensorless control using high-frequency signal injection. Low-speed sensorless operation is forbiden here. FEM modeling.

IV. Local Saturation

In many papers during the last decade it was reported that the *dq*-model developed for PMSMs with integral-slot distributed windings is not reliable enough for TC-PMSMs. Experiments show that the output of the classical *dq*-model of PMSMs applied to TC-PMSMs differs from measurements [16], especially, in FW region of operation and at high loadings.

It is observed that, because of the TC-windings, the saturation of TC-PMSMs is position- and time-dependent under the influence of current linkage sub-harmonics. In [17] it is reported that inductances of TC-PMSMs vary with the rotor position. This inductance variation is caused mainly by local saturation effects due to the asynchronous harmonic magnetic fluxes. For TC-SPMSMs the effect of harmonic fluxes is limited by a high effective air gap length. Whereas, in TC-IPMSMs the saturation produced by the harmonic fluxes can be noticeable. Iron saturation is the fundamental cause for the torque ripple in TC-PMSMs [18].

In Fig. 6 it can be seen that the inductance maps are not symmetrical with the positive and negative values of

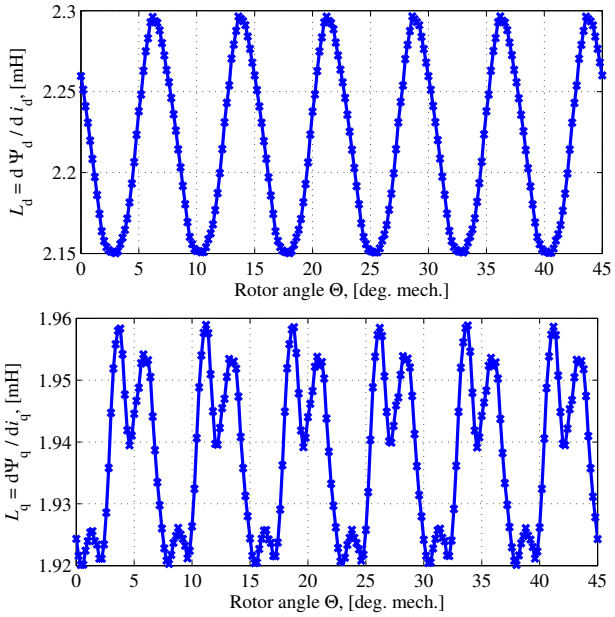

Fig. 9. Direct-axis differential inductance L_d variation (top) and quadrature-axis differential inductance L_q variation (bottom) with the rotor position during one electrical period (for 18/16 machine it corresponds to 45 mechanical degrees rotation). FEM modeling. Sinusoidal current supply, $i_\mathrm{d} = -30$ A and $i_\mathrm{q} = 120$ A.

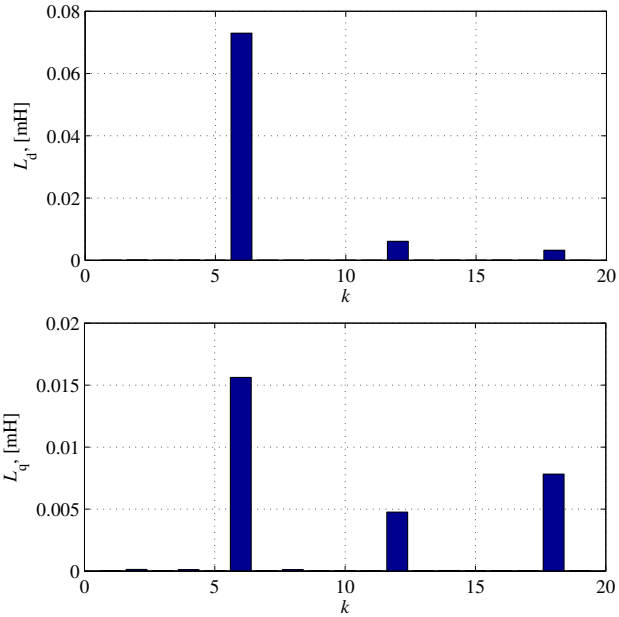

Fig. 10. Direct differential inductance L_d variation spectrum (top) and quadrature differential inductance L_q variation spectrum (bottom) at operating point captured during one electrical period. FEM modeling. The peak-to-peak inductance ripple is 7 %.

quadrature-axis current in both L_d and L_q as the case usually is for low-torque-density machines with $q > 1$ [5]. Usually, inductance maps are obtained with FEM when the direct or quadrature rotor axis is aligned with the geometrical magnetic axis of a phase. Maps in Fig. 6 were obtained when the rotor position was not aligned with the geometrical magnetic axis of a stator phase as it is shown in Fig. 4.

Fig. 9 shows the variations of the *d*- and *q*-axes inductances at different rotor positions at $i_\mathrm{d} = -30$ A and $i_\mathrm{q} = 120$ A. The d-axis inductance varies almost sinusoidally with the magnitude $L_\tau = 0.07$ mH.

This inductance variation induces an alternating voltage U_dL in the windings. The value of this induced voltage can be estimated by

$$U_\mathrm{dL} = i_\mathrm{d}\frac{\mathrm{d}L_\mathrm{d}}{\mathrm{d}t} = i_\mathrm{d}\frac{\mathrm{d}L_\tau \sin(k\omega t)}{\mathrm{d}t}. \tag{12}$$

The RMS value of this varying voltage at working point when i_d = -30 A and i_q = 120 A is

$$U_\mathrm{dL} = i_\mathrm{d}\frac{L_\tau}{\sqrt{2}}k2\pi f = 30\mathrm{A}\frac{0.07\mathrm{mH}}{\sqrt{2}}6\ 2\pi 200\mathrm{Hz} = 11.2\mathrm{V}, \tag{13}$$

which is higher than the resistive voltage drop of this machine $R_\mathrm{s}i_\mathrm{s} \approx 7$ V. Therefore, for the precise control, this inductance variation should be taken into account.

The inductance varies because of the local temporal saturation caused by interaction of the travelling current linkage harmonics with the magnetic flux waveform of the rotor. At an instant depicted in Fig. 2, when maximum current is flowing in the phase U, the 4^th and the 5^th harmonics contribute the most to the current linkage under teeth 2–4 (phase U). This current linkage induces the magnetic flux which, together with the magnetic flux of the PMs, locally saturates the iron core in and below the teeth 2–4. This saturation decreases the inductance in the phase U and contributes to inductance variation along the *dq*-axes. Such a situation repeats 6 times during one electrical period for three phases and positive and negative peaks of the phase currents. That is the 6^th harmonic is produced in the spectra of the inductance variation waveforms during one electrical period (see Fig. 10).

As it can be noticed in Fig.10, the 6^th harmonic pulses are the dominating pulses in the inductance variations. Therefore, the inductance variation pulses are caused by the saturation due to the travelling harmonics in the gap.

From the spectra of the inductance variations the 12^th and 18^th harmonics are also noticeable in the *d*- and *q*-axes inductances. These variations are due to the interaction of the synchronous flux wave of the rotor and the 2^nd and the 5^th current linkage harmonics travelling to the opposite direction

$$k = 2(\nu_\mathrm{syn} - (-\nu_2)) = 2(4 - (-2)) = 12, \tag{14}$$

$$k = 2(\nu_\mathrm{syn} - (-\nu_5)) = 2(4 - (-5)) = 18, \tag{15}$$

where factor 2 is due to the fact that saturation can be produced by the intersection of the positive half-waves of the synchronous and the first current linkage harmonics as well as by the intersection of the negative half-waves.

The slotting effect also causes variation of the *d*- and *q*-axes inductances. The slotting introduces intrinsic magnetic anisotropy of the stator bore which results in cogging torque produced by reluctance forces due to anisotropy (see Fig. 14). The harmonic ordinal of this variation k_cog during one electrical period can be determined according to [19]

$$k_\mathrm{cog} = \frac{\mathrm{lcm}(Q_\mathrm{s}, 2p)}{p}, \tag{16}$$

where lcm is the least common multiplier, Q_s is the number of stator slots, and p is the number of pole pairs. For 18/16

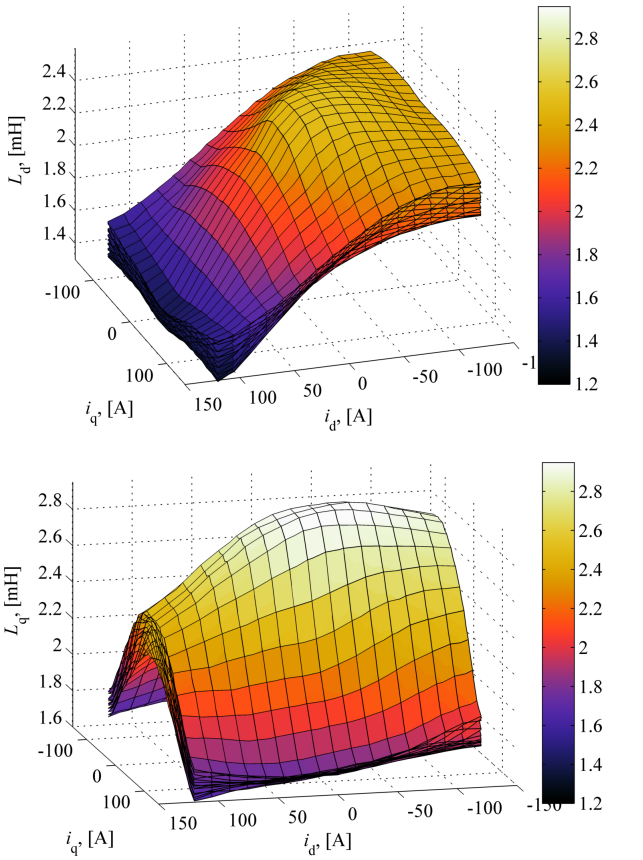

Fig. 11. Sets of direct differential inductance $L_{\mathrm{d}}(i_{\mathrm{d}}, i_{\mathrm{q}})$ maps (top) and quadrature differential inductance $L_{\mathrm{q}}(i_{\mathrm{q}}, i_{\mathrm{d}})$ maps (bottom) obtained at different rotor positions during one electrical period. Maximum discrepancy at high current values is 12 %. FEM modeling. Sinusoidal current supply.

machine $k_{\mathrm{cog}} = 18$. Therefore, the 18^{th} harmonic in the d- and q-axes inductances of the 18/16 machine is caused both – by local temporal harmonic saturation, and by stator anisotropy.

Fig. 11 shows a set of direct and quadrature differential inductance maps obtained at different rotor positions. These inductance variations are not included in the classical dq-model of PMSM. Therefore, a TC-PMSM can not be precisely represented by an inductance map obtained at a single rotor position.

Fig. 12 shows the magnitude of inductance variation in percents of $L_{\mathrm{d}}(i_{\mathrm{q}}, i_{\mathrm{d}})$ and the amplitude of $L_{\tau\mathrm{d}}(i_{\mathrm{q}}, i_{\mathrm{d}})$. It can be noticed that at low currents the inductance almost has no variation, but at higher currents the magnitude of inductance variation increases significantly. This inductance variation should be considered when choosing the forbidden region for sensorless HF signal injection (see Fig. 8). Higher safety limit should be chosen.

Fig. 13 shows the magnitude of the inductance variation in percents of $L_{\mathrm{q}}(i_{\mathrm{q}}, i_{\mathrm{d}})$. The L_{q} inductance variation along $i_{\mathrm{d}} = 0$ A is very low, and, therefore, can be neglected for this particular machine shown in Fig. 4, which has thin iron webs. With MTPA control, which trajectory is usually close to the $i_{\mathrm{d}} = 0$ with moderate negative d-axis current component, the q-axis inductance can also be assumed as constant along the stator bore. However, the d-axis inductance variation can not be neglected for this particular TC-PMSM.

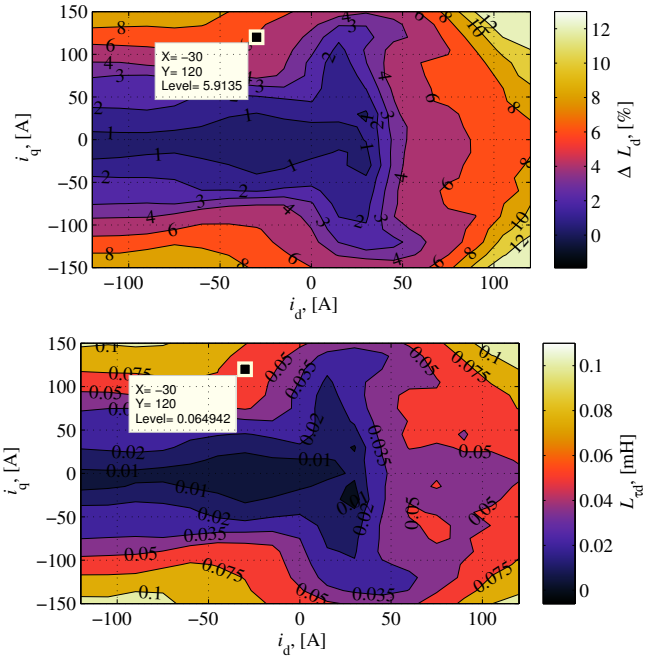

Fig. 12. Direct inductance variation map in percents of L_{d} (top) and direct inductance variation magnitude $L_{\tau\mathrm{d}}$ (bottom). FEM computation.

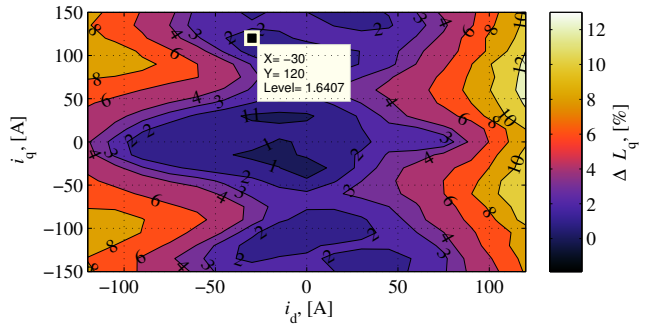

Fig. 13. Quadrature inductance variation map in percents of L_{q}. FEM computation.

V. Torque Quality

Torque quality can be assessed by cogging torque and torque ripple. The cogging torque is the pulsating torque due to the permanent magnet flux and angular magnetic anisotropy of the stator. The ripple torque is due to interaction of the stator current linkage and the rotor electromagnetic properties (saliency, saturation and PM flux linkage).

Fig. 14 shows the cogging torque of the 18/16 machine during one electrical period. The harmonic decomposition of the cogging torque is also shown. The 18^{th} slotting harmonic is clearly seen. The magnitude of the cogging for this TC-IPMSM is negligibly small.

The cogging torque can be decreased by diminishing the stator magnetic anisotropy – by skewing, decreasing the slot openings, using IPM rotor, increasing the air gap or by using semi-magnetic wedges. The cogging torque can be ultimately eliminated if slotless windings (air gap windings) are used. However, the last measure is only theoretical for industrial high-torque machines as it significantly lowers the air gap flux density and, therefore, decreases the torque density.

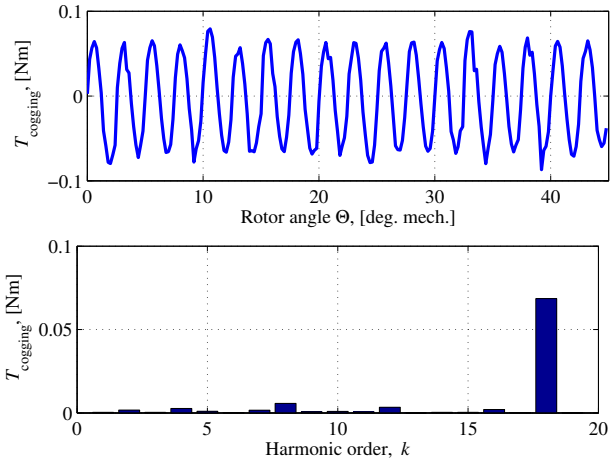

Fig. 14. Cogging torque due to angular anysotropy (slotting) of the stator (top) and cogging torque harmonics (bottom). FEM simulation during one electrical cycle, i = 0.

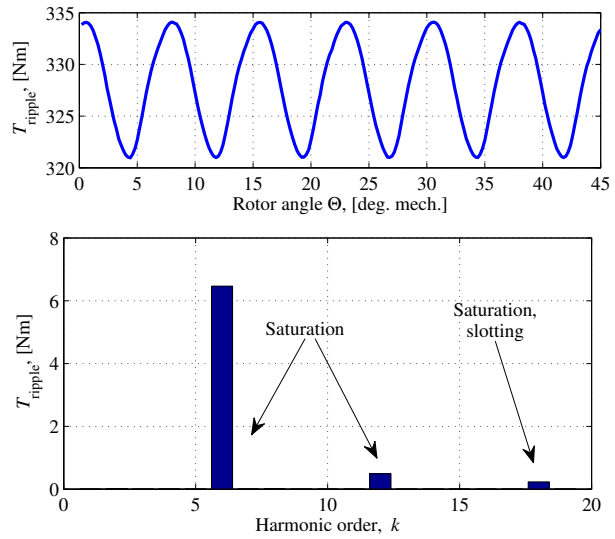

Fig. 15. Pulsating torque at nominal operating point (top) and harmonics of the pulsating torque (bottom). FEM simulation during one electrical cycle, i_{d} = -30 A and i_{q} = 120 A.

Fig. 15 shows the torque profile of the loaded 18/16 TC-IPMSM during one electrical period at operating point when i_{d} = -30 A and i_{q} = 120 A. The torque harmonic content is also shown.

The magnitude of $k = 12$ torque harmonic is very small as the $\nu = -2$ current linkage harmonic has relatively small magnitude. The magnitude of $k = 18$ torque harmonics is also low because of the low contribution of the cogging and local saturation. The pole-pitch of the corresponding current linkage harmonic $\nu = -5$ is short and the saturation is not so apparently localized. The dependence of the torque from the dq-axes inductances can be seen from equations (3)–(5).

At higher currents the sub-harmonic saturation is deeper and the torque ripple magnitude will also be higher. At low currents, when the machine is operated at linear magnetic region, only the cogging torque frequencies can be observed in the torque waveform due to the absence of saturation.

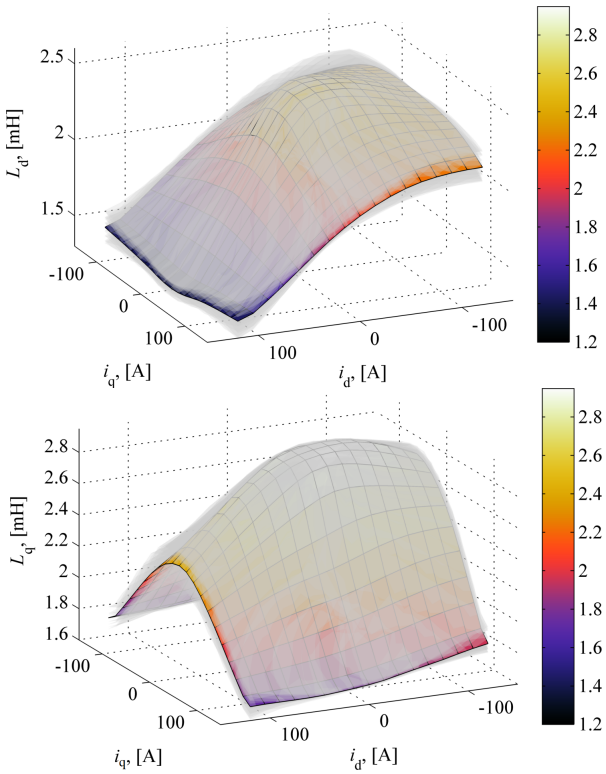

Fig. 16. Averaged inductance maps along with transparent inductance maps at different rotor positions.

VI. Improved dq-model for TC-PMSMs

One possible way to avoid problems with inductance variation along the stator bore due to the harmonics is to design a machine which will not be vulnerable to saturation. It means that the operating point of the machine should be placed well below the point where saturation starts – meaning in practice thicker teeth and yokes and lower values of the flux density in the machine. This, however, decreases the torque and power densities of the machine, which is not desirable, especially, in mobile applications, such as hybrid electric vehicles or aviation. In these applications high-torque-density electrical machines are required.

The classical dq-model can still be used if the inductance variation is not very significant. It happens, for example, when machine operation region mainly lies below the point where saturation becomes noticeable.

If a smooth torque output is not the main requirement from the machine, the inductance variation along the stator bore can be neglected. The inductance can be approximated with a certain level of accuracy by using averaged inductance maps along the stator bore (see Fig. 16).

However, when the inductance variation, as a function of position and time, is significant (which should be valid for high-torque- and high-power-density machines), and the smooth torque production is desired, the inductance variation should be directly modelled in the equivalent circuits of d- and q-axes in order to obtain smooth output torque. At least the most significant inductance variations $L_{\tau \mathrm{d}6}\cos(6\omega t + \phi_{\mathrm{d}})$ and $L_{\tau \mathrm{q}6}\cos(6\omega t + \phi_{\mathrm{q}})$ should be included [20]. When current linkage harmonic saturation is taken into account the d-axis

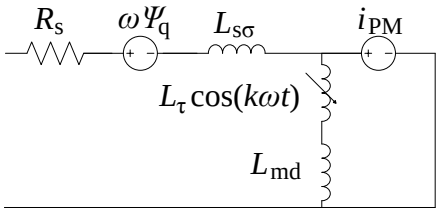

Fig. 17. Equivalent circuit along the d-axis of TC-PMSM taking the saturation-caused inductance variation into account.

can be represented by an equivalent circuit in Fig. 17.

The magnitudes of $L_{\tau \mathrm{d}6}$ and $L_{\tau \mathrm{q}6}$ are dependent on the magnetic state of the machine and additional inductance maps should be calculated beforehand for $L_{\tau \mathrm{d}6}(i_\mathrm{d}, i_\mathrm{q})$ and $L_{\tau \mathrm{q}6}(i_\mathrm{d}, i_\mathrm{q})$. Information for $L_{\tau \mathrm{d}6}$ and $L_{\tau \mathrm{q}6}$ can be taken using similar maps as shown in Fig. 12.

Voltage equation for the d-axis becomes

$$U_\mathrm{d} = R_\mathrm{s} i_\mathrm{d} + L_\mathrm{d} \frac{\mathrm{d}i_\mathrm{d}}{\mathrm{d}t} + i_\mathrm{d} \frac{\mathrm{d}L_\mathrm{d}}{\mathrm{d}t} - \omega \Psi_\mathrm{q}, \tag{17}$$

$$U_\mathrm{d} = R_\mathrm{s} i_\mathrm{d} + L_\mathrm{d} \frac{\mathrm{d}i_\mathrm{d}}{\mathrm{d}t} + i_\mathrm{d} L_{\tau \mathrm{d}6} \frac{\mathrm{d}\cos(6\omega t + \phi_\mathrm{d})}{\mathrm{d}t} - \omega \Psi_\mathrm{q}, \tag{18}$$

and for the q-axis

$$U_\mathrm{q} = R_\mathrm{s} i_\mathrm{q} + L_\mathrm{q} \frac{\mathrm{d}i_\mathrm{q}}{\mathrm{d}t} + i_\mathrm{q} \frac{\mathrm{d}L_\mathrm{q}}{\mathrm{d}t} + \omega \Psi_\mathrm{d}, \tag{19}$$

$$U_\mathrm{q} = R_\mathrm{s} i_\mathrm{q} + L_\mathrm{q} \frac{\mathrm{d}i_\mathrm{q}}{\mathrm{d}t} + i_\mathrm{q} L_{\tau \mathrm{q}6} \frac{\mathrm{d}\cos(6\omega t + \phi_\mathrm{q})}{\mathrm{d}t} + \omega \Psi_\mathrm{d}. \tag{20}$$

When localized sub-harmonic saturation plays a significant role in the operation of a machine, this approach should be used for the precise modeling of the machine behavior. This model can be used together with torque ripple minimisation techniques using active stator current excitation to compensate the torque pulsations [21]–[23].

VII. Conclusions

In this paper it was shown that torque quality is strongly dependent on the saturation caused by the asynchronous current linkage harmonics. These harmonics locally saturate the stator core which results in the inductance variation along the d- and q- magnetic axes. This inductance variation should be taken into account during the design process of the machine, and in control design for TC-PMSM drives, particularly for sensorless control schemes.

The high-torque- and high-power-density TC-PMSMs are especially vulnerable to the rotating current linkage harmonic saturation as these machines work at high values of flux density and the localised saturation is especially apparent in this case.

References

[1] P. Ponomarev, P. Lindh, and J. Pyrhonen, "Effect of slot-and-pole combination on the leakage inductance and the performance of tooth-coil permanent-magnet synchronous machines," *Industrial Electronics, IEEE Transactions on*, vol. 60, no. 10, pp. 4310–4317, 2013.

[2] F. Magnussen and H. Lendenmann, "Parasitic effects in pm machines with concentrated windings," *Industry Applications, IEEE Transactions on*, vol. 43, no. 5, pp. 1223–1232, 2007.

[3] N. Bianchi, S. Bolognani, and E. Fornasiero, "An overview of rotor losses determination in three-phase fractional-slot pm machines," *Industry Applications, IEEE Transactions on*, vol. 46, no. 6, pp. 2338–2345, Nov.-Dec.

[4] P. Ponomarev, M. Polikarpova, O. Heinikainen, and J. Pyrhonen, "Design of integrated electro-hydraulic power unit for hybrid mobile working machines," in *Power Electronics and Applications (EPE 2011), Proceedings of the 2011-14th European Conference on*, 30 2011-Sept. 1, pp. 1–10.

[5] M. Rilla, *Design of Salient Pole PM Synchronous Machines for a Vehicle Traction - Analysis and implementation*. Lappeenranta, Finland: Doctpral dissertation, Lappeenranta University of Technology, 2012.

[6] L. Alberti, M. Barcaro, and N. Bianchi, "Design of a low torque ripple fractional-slot interior permanent magnet motor," in *Energy Conversion Congress and Exposition (ECCE), 2012 IEEE*, Sept., pp. 509–516.

[7] C. Dufour, S. Cense, T. Yamada, R. Imamura, and J. Belanger, "Fpga permanent magnet synchronous motor floating-point models with variable-dq and spatial harmonic finite-element analysis solvers," in *Power Electronics and Motion Control Conference (EPE/PEMC), 2012 15th International*, sept. 2012, pp. LS6b.2–1 –LS6b.2–10.

[8] B. Stumberger, G. Stumberger, D. Dolinar, A. Hamler, and M. Trlep, "Evaluation of saturation and cross-magnetization effects in interior permanent-magnet synchronous motor," *Industry Applications, IEEE Transactions on*, vol. 39, no. 5, pp. 1264 – 1271, sept.-oct. 2003.

[9] A. Consoli, G. Scarcella, G. Scelba, and A. Testa, "Steady-state and transient operation of ipmsms under maximum-torque-per-ampere control," *Industry Applications, IEEE Transactions on*, vol. 46, no. 1, pp. 121–129, 2010.

[10] S.-Y. Jung, J. Hong, and K. Nam, "Current minimizing torque control of the ipmsm using ferrari's method," *Power Electronics, IEEE Transactions on*, vol. 28, no. 12, pp. 5603–5617, 2013.

[11] T. Matzen and P. Rasmussen, "Sensorless characteristics of hybrid pm machines at zero and low speed," in *Energy Conversion Congress and Exposition, 2009. ECCE 2009. IEEE*, Sept., pp. 2374–2380.

[12] S.-K. Sul and S. Kim, "Sensorless control of ipmsm: Past, present, and future," *IEEJ Journal of Industry Applications*, vol. 1, no. 1, pp. 15–23, 2012.

[13] Y. Kano, T. Kosaka, N. Matsui, and T. Nakanishi, "Sensorless-oriented design of ipm motors for general industrial applications," in *Electrical Machines, 2008. ICEM 2008. 18th International Conference on*, 2008, pp. 1–6.

[14] P. Sergeant, F. De Belie, and J. Melkebeek, "Rotor geometry design of interior pmsms with and without flux barriers for more accurate sensorless control," *Industrial Electronics, IEEE Transactions on*, vol. 59, no. 6, pp. 2457–2465, 2012.

[15] N. Bianchi and S. Bolognani, "Sensorless-oriented design of pm motors," *Industry Applications, IEEE Transactions on*, vol. 45, no. 4, pp. 1249–1257, 2009.

[16] N. Dai, R. Dutta, and M. Rahman, "Comparative performance analysis of field-oriented control and direct torque control for a fractional-slot concentrated winding interior permanent magnet synchronous machine," in *Electrical Machines (ICEM), 2012 XXth International Conference on*, sept. 2012, pp. 879 –885.

[17] E. Schmidt and M. Susic, "Finite element analysis of permanent magnet synchronous machines with fractional slot tooth coil windings," *Elektrotechnik und Informationstechnik*, vol. 128, no. 3, pp. 86–94, 2011.

[18] M. Barcaro, N. Bianchi, and F. Magnussen, "Remarks on torque estimation accuracy in fractional-slot permanent-magnet motors," *Industrial Electronics, IEEE Transactions on*, vol. 59, no. 6, pp. 2565 –2572, june 2012.

[19] Z. Zhu and D. Howe, "Influence of design parameters on cogging torque in permanent magnet machines," *Energy Conversion, IEEE Transactions on*, vol. 15, no. 4, pp. 407–412, 2000.

[20] W. Qian, J. X. Xu, and S. Panda, "Periodic torque ripples minimization in pmsm using learning variable structure control based on a torque observer," in *Industrial Electronics Society, 2003. IECON '03. The 29th Annual Conference of the IEEE*, vol. 3, 2003, pp. 2983–2988 Vol.3.

[21] G.-H. Lee, "Active cancellation of pmsm torque ripple caused by magnetic saturation for eps applications," *Journal of Power Electronics*, vol. 10, no. 2, pp. 176–180, 2010.

[22] J. Holtz and L. Springob, "Identification and compensation of torque ripple in high-precision permanent magnet motor drives," *Industrial Electronics, IEEE Transactions on*, vol. 43, no. 2, pp. 309–320, 1996.

[23] V. Petrovic, R. Ortega, A. Stankovic, and G. Tadmor, "Design and implementation of an adaptive controller for torque ripple minimization in pm synchronous motors," *Power Electronics, IEEE Transactions on*, vol. 15, no. 5, pp. 871–880, 2000.